MRI-Guided Cardiac RF Ablation for Comparing MRI Characteristics of Acute Lesions and Associated Electrophysiologic Voltage Reductions

Philippa R. P. Krahn, Labonny Biswas, Sebastian Ferguson, Venkat Ramanan, Jennifer Barry, Sheldon M. Singh, Mihaela Pop, and Graham A. Wright

Abstract*—*Objective: **Radiofrequency (RF) energy delivered to cardiac tissue produces a core ablation lesion with surrounding edema, the latter of which has been implicated in acute procedural failure of Ventricular Tachycardia (VT) ablation and late arrhythmia recurrence. This study sought to investigate the electrophysiological characteristics of acute RF lesions in the left ventricle (LV) visualized with native-contrast Magnetic Resonance Imaging (MRI).** ***Methods:*** **An MR-guided electrophysiology system was used to deliver RF ablation in the LV of 8 swine (9 RF lesions in total), then perform MRI and electroanatomic mapping. The permanent RF lesions and transient edema were delineated via native-contrast MRI segmentation of T1-weighted images and T2 maps respectively. Bipolar voltage measurements were matched with image characteristics of pixels adjacent to the catheter tip. Native-contrast MR visualization was verified with 3D late gadolinium enhanced MRI and histology.** ***Results:*** **The T2-derived edema was significantly larger than the T1-derived RF lesion (2.1$\pm$1.5 mL compared to 0.58$\pm$0.34 mL; p=0.01). Bipolar voltage was significantly reduced in the presence of RF lesion core ($p<0.05$) and edema ($p<0.05$), with similar trends suggesting that both the permanent lesion and transient edema contributed to the region of reduced voltage. While bipolar voltage was significantly decreased where RF lesions are present ($p<0.05$), voltage did not change significantly with lesion transmurality ($p>0.05$).** ***Conclusion:*** **Permanent RF lesions and transient edema are distinct in native-contrast MR images, but not differentiable using bipolar voltage.** ***Significance:*** **Intraprocedural native-contrast MRI may provide valuable lesion assessment in MR-guided ablation, whose clinical application is now feasible.**

***Index Terms*—Cardiac arrhythmia, image-guided interventions, magnetic resonance imaging, RF ablation.**

Manuscript received August 11, 2021; revised December 21, 2021; accepted February 5, 2022. Date of publication February 16, 2022; date of current version July 19, 2022. This work was supported in part by GE Healthcare, HeartVista, Imricor Medical Systems, the Canadian Institutes of Health Research under Grant MOP-93531, the Federal Development Agency of Canada, and the Government of Ontario. *(Corresponding author: Philippa R. P. Krahn.)*

Philippa R. P. Krahn is with the Sunnybrook Research Institute, Toronto, ON M4N3M5, Canada and also with the Department of Medical Biophysics, University of Toronto, Toronto, ON M4N3M5, Canada (e-mail: philippa.krahn@gmail.com).

Graham A. Wright is with the Sunnybrook Research Institute, Canada and also with the Department of Medical Biophysics, the University of Toronto, Canada.

Labonny Biswas, Sebastian Ferguson, Venkat Ramanan, Jennifer Barry, and Mihaela Pop are with the Sunnybrook Research Institute, Canada.

Sheldon M. Singh is with the Department of Medicine, the University of Toronto, Canada and also with the Schulich Heart Program in Sunnybrook Health Sciences Centre, Canada.

Digital Object Identifier 10.1109/TBME.2022.3152145

I. Introduction

RADIOFREQUENCY (RF) ablation is an effective therapy for scar-related Ventricular Tachycardia (VT) [1], [2]. One challenge associated with VT ablation procedures is obtaining complete conduction block within VT reentry circuits, the arrhythmogenic substrates which are targeted for RF ablation. A method of identifying the permanence of delivered ablation lesions is needed in order to ensure complete elimination of the reentry circuit, and to prevent early and late arrhythmia recurrence.

Several preclinical and clinical studies of ablation in the atria have suggested that the development of edema (fluid accumulation associated with inflammation surrounding the ablation site) impacts procedural endpoints and recurrence [3]–[6]. It is likely that edema formation at the time of a VT ablation procedure may result in acute procedure success only to allow for late arrhythmia recurrence [7]. The contribution of edema to acute electrophysiologic properties highlights the limitation of solely using electrophysiological endpoints when performing intraprocedural evaluation of ablation.

Magnetic Resonance Imaging (MRI) can directly visualize therapeutic RF ablation lesions in vivo [8], [9] thereby providing a valuable method of assessing acute lesions and the completeness of ablation. Specifically, native MR contrast (without the injection of contrast agent) can visualize RF lesions and edema via changes to endogenous myocardial T1 and T2 respectively [10]–[13]. Native T1 MRI contrast reveals tissue which has undergone a heat-induced transformation of the perfusing blood to a paramagnetic form (above approximately 50 °C) [14], and which is associated with coagulative necrosis [10]. The extent of the thermal lesion enhanced in native T1-weighted MRI correlates with the chronic extent of the lesion [12],

suggesting that this contrast represents the permanent lesion. Native T2 contrast reflects increased fluid associated edema as part of the physiologic response after RF ablation, and this T2-derived edema appears to be transient, resorbing within days after ablation [11]. However, is not yet well understood how MR visualization of acute therapeutic RF lesions may relate to the functional electrophysiologic properties (such as bipolar voltage) of corresponding tissue during the time frame of an ablation procedure.

A major added value of MR imaging of RF lesions is the ability to directly visualize lesion geometry. This study uniquely investigates bipolar voltage within MRI-derived RF ablation lesions. By using a novel integrated MR-guided EP system, the potential for error associated with registering data acquired in separate MRI and EP systems was reduced, and the time delay between each acquisition was minimized. Ablations were performed in the left ventricle (LV) of a preclinical swine model, extending previous investigations of ablation in thinner cardiac chambers (atria or RV) [9], [15]. Both the permanent RF lesion core and edema were probed, each of which are clinically relevant as they represent permanent and transient injury respectively. The acute composition of ablated tissue was evaluated using native (non-contrast-enhanced) MR images, which can be acquired repeatedly throughout an ablation procedure [16], when an understanding of RF lesion characteristics may be most critical to clinical decision-making. As a result, the current study has particular relevance for further development of MR-guided EP.

In this context, we hypothesize that (1) RF lesions visualized by MR are associated with suppressed bipolar voltage, (2) both the permanent lesion core and edema derived from MRI contribute to the region of suppressed voltage, and (3) the permanent lesion core and transient edema are distinguishable by MR but not by electrophysiological criteria. A preliminary version of this work has been reported [17]–[19].

II. Methods

A. Animal Preparation

MR-guided ablation was performed in 8 healthy Yorkshire swine (62±17 kg). Each animal was given intramuscular injections of ketamine (33 mg/kg) and atropine (0.05 mg/kg), then isoflurane gas (1–5%) was delivered continuously to maintain anesthesia. To mitigate arrhythmia, a bolus of amiodarone (75 mg) was given prior to catheter insertion and lidocaine (20 mg) was administered as needed throughout the studies. All study protocols were approved by the institutional Animal Care Committee.

B. MR-Guided Endocardial Ablation

Studies were performed entirely within a 1.5 T wide-bore MR scanner (GE MR450 w), with a 4-channel cardiac array coil used for imaging. 2D cine balanced steady-state free precession (SSFP) images acquired in standard short- and long-axis views were used as anatomical roadmaps for the intervention (20 cardiac phases across 1 R-R interval, repetition time (TR)/echo time (TE)=5/2 ms, resolution=1.4×1.6 mm^2, slice thickness=6 mm).

TABLE I
RF Ablation Parameters and Data Acquired During MR-Guided Electroanatomic Mapping

Animal #	Ablation #	RF power (W)	Duration (s)	# EGMs
1	1, 2	30, 30	60, 60	80
2	3	30	90	101
3	4	30	100	104
4	5	35	120	115
5	6	30	90	176
6	7	35	90	129
7	8	35	120	200
8	9	35	120	195

The MR-EP system used for the ablation procedures has been described in detail previously [16], [20], [21]. Briefly, a 9F electrophysiology and ablation catheter (Vision-MR; Imricor Medical Systems) was actively tracked using a projection MRI sequence [22] (field of view (FOV)=60 cm, matrix=512, flip angle=5°, TR=14.3 ms, tracking rate=23 fps) implemented in RTHawk (HeartVista Inc.). Vurtigo (image-guided cardiac intervention software developed in-house) [23] was used to visualize the catheter in real time as it was moved within the MRI coordinate frame, with respect to the anatomical cine MR images. This navigation visualization in Vurtigo and EP traces (in the Advantage-MR software; Imricor) were displayed for the operator on MR-compatible monitors placed adjacent to the magnet bore.

The catheter was advanced through the carotid artery to the LV, where endocardial ablations were delivered with 17 mL/min irrigation and ablation parameters listed in Table I (1500 T14 generator, St. Jude Medical). The catheter location was actively tracked throughout ablation. An Expression MR Patient Monitor (Invivo Corp.) was used for monitoring ECG, end-tidal CO_2, and peripheral capillary oxygen saturation throughout the procedure.

C. Imaging Protocol

RF ablation lesions were primarily visualized using native-contrast (non-contrast-enhanced) MR. Lesion assessment images were all acquired in the standard short-axis orientation to capture the maximum extent of the RF lesions while minimizing partial volume effects. A stack of several image slices was acquired, centred at the known site of ablation (the catheter location during RF ablation delivery). A previously validated spiral sequence with T2 preparation was used for parametric T2 mapping to visualize water accumulation associated with edema after ablation (TE=2.9, 24.3, 45.6, 184.2 ms, TR=2 R-R intervals, typical heart rate=87 bpm, 10 spiral interleaves each with 3072 points, in-plane resolution=1.3×1.3 mm^2, slice thickness=6 mm) [24]. This was followed by a native T1-weighted inversion-recovery SSFP (IR-SSFP) sequence [25] to visualize the thermal core of ablation [10] (diastolic phase selected from 40 phases acquired across 2 R-R intervals, views per segment=16, TR/TE=5/2 ms, in-plane resolution=1.4×1.6 mm^2, slice thickness=6 mm). To verify the pattern of ablation, a bolus of Gd-DTPA (0.2 mml/kg, Magnevist, Bayer Healthcare Pharmaceuticals) was injected for

3D late gadolinium enhancement (LGE) imaging with respiratory navigation in a subset of 5 animals (14 min post-injection, inversion time (TI)=300 ms, resolution=$1.1\times1.1\times2.6$ mm^3, TR/TE=5/2 ms).

D. MR-Guided Electroanatomic Voltage Mapping

Electroanatomic mapping (EAM) was performed within the MR scanner using the MR-EP system to acquire bipolar voltage maps of the LV endocardium after ablation. Intracardiac electrograms (EGMs) were recorded in sinus rhythm, according to the following qualitative criteria: stable QRS morphology and cycle length for $\geq$2 heartbeats, near-field signal, and LV wall proximity. Each point recording comprised simultaneous EGM, ECG, catheter tip locations, and respiratory phase surrogate over approximately 5 s. EGM sampling was performed throughout the LV, but with the greatest sampling density near the recorded catheter tip location during ablation. Catheter positions during EGM recordings were mapped to an LV endocardial surface shell derived from diastolic cine MR images. All data was acquired within the MRI coordinate frame and was inherently spatially co-registered. The median catheter position from each 5-s recording was used for offline analysis, after smoothing and gating to mid-diastole and end-expiration to match the cardiac and respiratory phases of static MR image acquisitions. The uncertainty (spatial spread) in catheter positions was a standard deviation (SD) of 2.2$\pm$0.9 mm on average across all recordings after gating.

E. Ex Vivo Tissue Examination

All animals were sacrificed after the MR-guided study. Explanted hearts were fixed in a 10% formalin solution then sliced to 4-mm slabs for inspection. Slabs which revealed the greatest extent of each lesion were used for RF lesion measurements. From these, the diameter of each RF lesion (the pale central core of the lesion) was manually measured by two expert observers. Slabs containing representative examples of lesions were sliced to 4-μm, stained with hematoxylin and eosin (H&E) and Masson's trichrome (MT), and scanned using a confocal laser microscope at 20$\times$ magnification.

F. Data Analysis and Statistics

T2 maps for edema visualization were generated using pixel-wise fitting to a validated 3-parameter model [26]. For native T1-weighted imaging to visualize RF lesion cores, an IR-SSFP image was selected in the diastolic cardiac phase at approximately TI=700–900 ms (previously determined to be optimal for lesion visualization) [10], [13]. This imaging sequence (and others with similar contrast) have consistently yielded RF lesion visualization which matches lesions seen in gross pathology [10], [13], [16], [31]. LV endo- and epicardial borders were manually delineated to identify the myocardium. Segmentation methods used for T1-derived RF lesions and T2-derived edema were originally described in [16]. The T1-derived lesion cores were regions with signal intensity at least 2 SD above a manually-drawn region in adjacent normal myocardium, a threshold that has been validated by strong agreement with manual segmentation [16]. The T2-derived edema was segmented based on regions with T2 at least 3 SD above a manually-drawn region in adjacent normal myocardium. Edema was identified as a single contiguous region. Morphological operations on the resulting mask included noise and spurious pixel removal, and filling in the edematous region while preserving borders. After segmentation, each image pixel within the LV could therefore be classified as healthy myocardium, lesion core, edema, or both (overlapping) core and edema. The volume and maximum diameter for each RF lesion and edematous region were determined from these segmentations. The reproducibility of RF lesion measurements from gross pathology was assessed using inter-observer variability with intraclass correlation coefficient (ICC).

MR and EP data were analyzed offline after the MR-guided studies. Each catheter recording was matched with the MR-derived tissue classification from LV pixels within the sensitive volume around the catheter tip (approximately 6 mm in radius) [27] and lesion transmurality. MATLAB (R2017b, MathWorks, Inc., Natick, Massachusetts) was used for image analysis and fusing MR and EP data. The association between bipolar voltage amplitude and corresponding MR image characteristics for each catheter recording was evaluated using linear mixed-effects models (LMMs) in R (version 3.3.3, lme4 package), including individual animal as a random effect. Continuous variables are expressed as mean $\pm$ SD unless stated otherwise. All tests were 2-sided, and $p<0.05$ was considered significant.

III. Results

A. MR Visualization of RF Lesions

RF ablation was performed in 8 animals, leading to the creation of 9 RF lesions. From native-contrast MRI, T2-derived edema typically encompassed the T1-derived lesion core (Fig. 1(A)–(C)) and was significantly larger in volume (2.1$\pm$1.5 mL compared to 0.58$\pm$0.34 mL; p=0.01, 2-sided t-test) and diameter (25.7$\pm$7.9 mm compared to 9.9$\pm$1.9 mm; $p<0.01$). Lesion dimensions are given in Table II. T1-weighted IR-SSFP images visualizing the RF lesion cores were acquired in diastole at TI=814$\pm$161 ms. The T1-weighted images and T2 maps used for this analysis were acquired at a median of 85 min (range: 65–245 min) and 80 min (range: 56–254 min) post-ablation respectively, to capture the full extent of edema after allowing sufficient time for it to develop [16]. Overall mean T2 was 44.1$\pm$15.5 ms in healthy myocardium, 59.5$\pm$14.0 ms in edematous regions, and 59.4$\pm$15.9 ms in the lesion cores. 3D LGE and gross pathology were used to verify the pattern of ablation in native-contrast MRI (Fig. 1(D)–(E)).

The volume of T1-derived lesion cores increased monotonically with the volume of T2-derived edema (Spearman's correlation coefficient r_s=0.86, p=0.02) and ablation power (r_s=0.85, p=0.04) but with no significant linear correlation (Pearson's r=0.54, 0.74, p=0.21, 0.06 respectively). However, this study is likely underpowered to detect these correlations as ablation parameters were not varied widely.

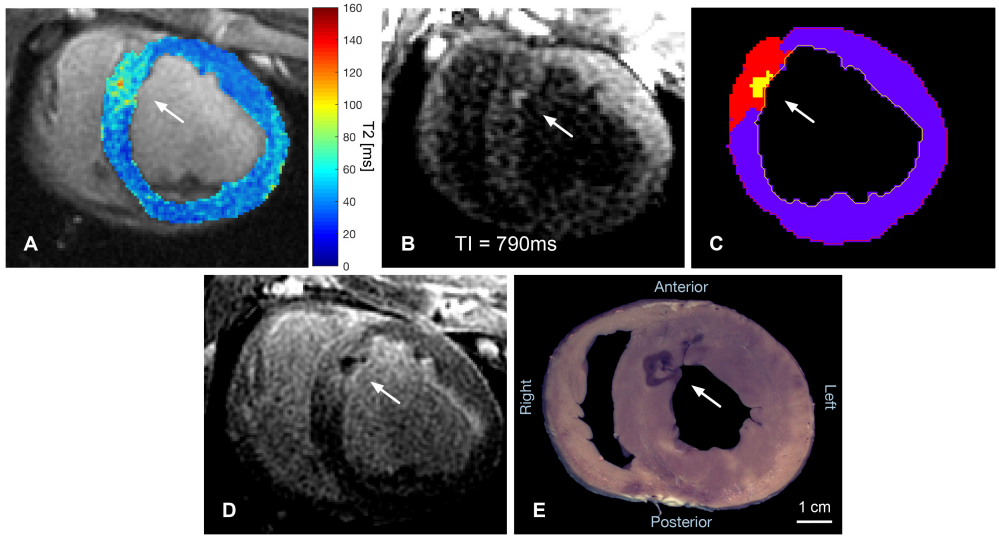

Fig. 1. MR visualization of an RF ablation lesion on the LV septal wall in a short-axis slice - (A) Parametric T2 map showing elevated T2 associated with edema (arrow). (B) T1-weighted IR-SSFP showing hyperenhancement (short T1) at the RF lesion core (arrow). (C) Combined segmentations from (A) and (B) (purple=myocardium, red=T2-derived edema, yellow=T1-derived lesion core). (D) 3D LGE, 14 min after gadolinium injection. (E) Gross pathology slice at a location corresponding to the MRI and cut in a similar short-axis orientation.

TABLE II
RF LESION DIMENSIONS MEASURED FROM MR IMAGES AND GROSS PATHOLOGY

		T2-derived edema		T1-derived lesion core		Gross pathology
Animal #	Ablation #	Volume (mL)	Diameter (mm)	Volume (mL)	Diameter (mm)	Diameter (mm)
1	1, 2	1.15, 1.71	20.92, 30.90	[a], [a]	[a], [a]	6.77, 6.52
2	3	0.30	20.19	0.09	9.31	8.08
3	4	2.92	31.76	0.54	10.14	11.93
4	5	2.53	23.28	1.20	12.40	12.11
5	6	0.62	13.91	0.41	9.88	7.13
6	7	2.04	23.22	0.24	8.59	7.36
7	8	5.29	41.08	0.74	9.30	6.53
8	9	2.46	26.48	0.43	8.63	7.43

[a]These lesions were small and not clearly apparent in these images.

B. Electroanatomic Mapping

During ablation, bipolar voltage dropped by approximately 50%. With the catheter held in a consistent position, the mean voltage was 6.2±3.4 mV immediately before then 2.6±0.7 mV immediately after ablation (p=0.01; paired t-test).

In 8 animals, EAMs were acquired after MR imaging and 116±35 min after ablation, showing bipolar voltage qualitatively within the LV, reflecting expected electrophysiological properties of tissue at the end of an ablation procedure. 1097 EGMs were recorded in total (137±46 EGMs per animal; Table I). After removing points >6 mm from the endocardial border or otherwise not satisfying the criteria described in *Methods*, 984 EGMs were used in analysis. EAMs consistently showed a spatial pattern of reduced bipolar voltage at and surrounding the ablation site (Fig. 2), with voltage near the ablation predominantly ≤3 mV, the threshold defined as abnormal in previous studies [28], [29].

C. MR-EP Correlation

Catheter recordings were matched with MR-derived tissue types adjacent to the catheter tip and within its sensitive FOV, as illustrated in Fig. 3(A). An LMM was used to evaluate bipolar voltage categorized by predominant tissue type within the catheter sensitive FOV. Bipolar voltage was significantly higher in healthy myocardium (3.8±1.9 mV) compared to the T2-derived edema (2.8±1.6 mV, p≪0.01). Voltages in the T1-derived lesion core (2.2±0.5 mV) approached a significant level of difference compared to the healthy myocardium (p=0.06), with this analysis constrained by the small number of samples containing predominantly lesion core. Voltages in the T2-derived edema and T1-derived core did not differ significantly (p>0.05). Intersubject SD was 0.43 mV.

A separate LMM was used to evaluate the relationship between bipolar voltages measured and the proportion of the catheter sensitive FOV occupied by the T1-derived lesion core and T2-derived edema, while accounting for differences between individual animals. The LMM indicated that bipolar voltage dropped with increasing proportions of both the T1-derived lesion core and the T2-derived edema within the catheter sensitive volume (Fig. 3(B)). Intersubject standard deviations were 0.36 mV and 0.41 mV for the LMMs evaluating voltage against the T1-derived lesion core and the T2-derived edema respectively. Voltages measured with 25-50% T1-derived lesion

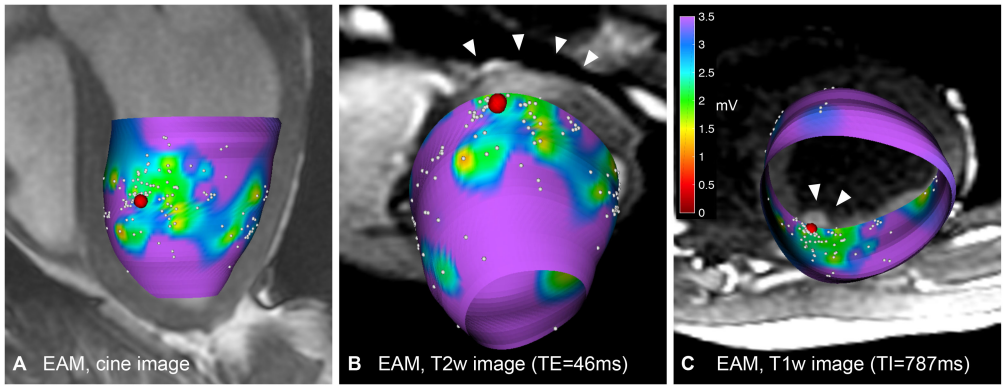

Fig. 2. EAM of the LV after ablation - (A) EAM overlaid on a cine image (red point=location of catheter tip during ablation, based on active MR tracking, white points=EGM recording sites). (B) Alignment between EAM and T2-weighted MR. Arrowheads indicate the approximate extent of edema (26.5 mm). (C) Alignment between EAM and T1-weighted MRI. Arrowheads indicate the approximate extent of the RF lesion (7.8 mm). EAMs all use the same color map (≥3.5 mV=purple, normal myocardium).

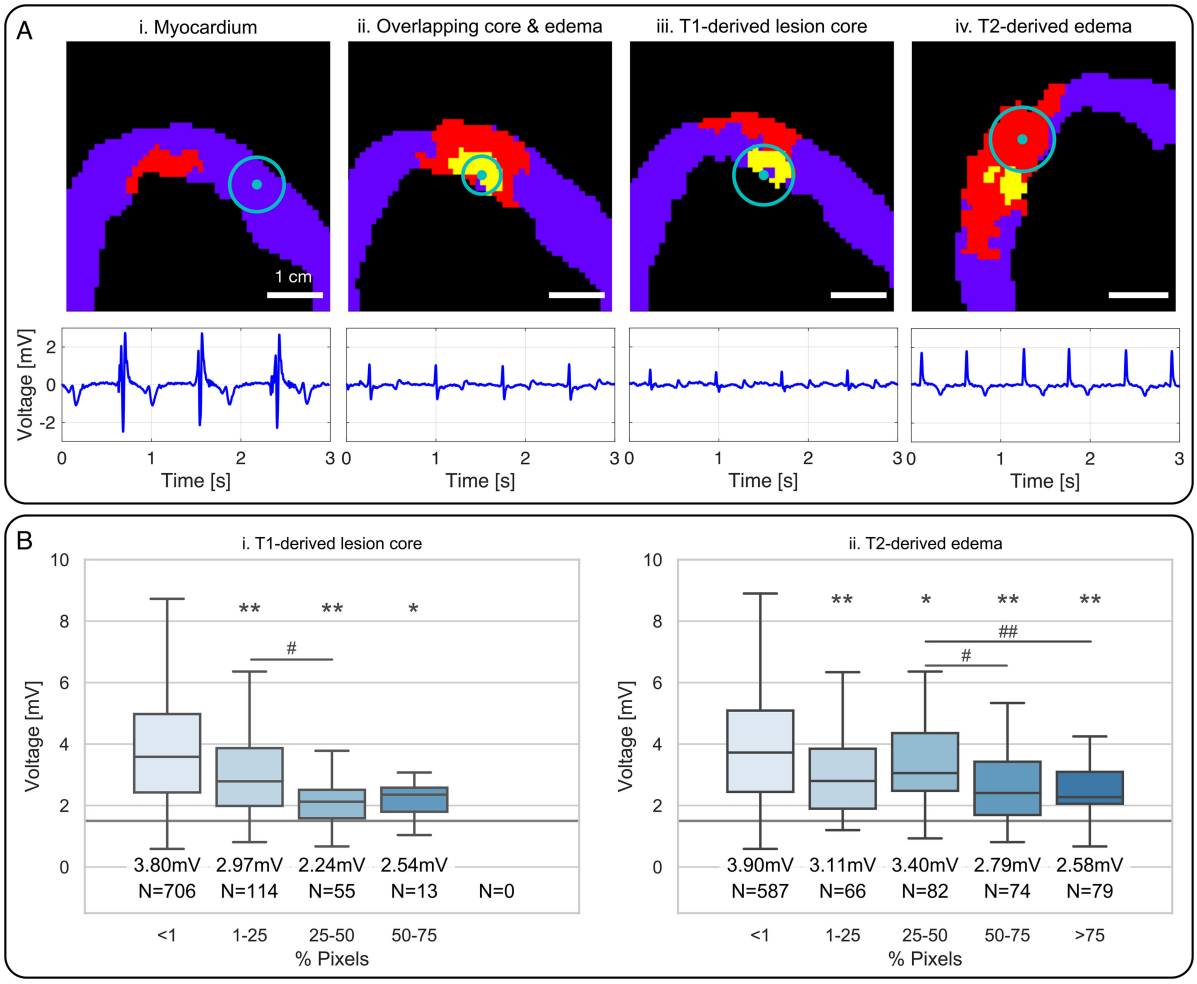

Fig. 3. Relationship between bipolar voltage and MR-derived tissue classification - (A) Catheter tip position during EGM recordings with respect to LV myocardium and RF lesions. The catheter tip position projected onto the image plane (cyan dot) and extent of its voltage-sensing FOV intersecting with the image plane (delineated in cyan) show the device contact with the LV segmented from MR (purple=myocardium, red=T2-derived edema, yellow=T1-derived lesion core). Scale bars=1 cm. The catheter tip within the myocardium likely represents a case where the catheter indented into the myocardial tissue. Corresponding EGMs are shown below each panel. (B) Bipolar voltage associated with catheter measurements where MR images showed varying proportions of nearby pixels belonging to the (i) T1-derived lesion core and (ii) T2-derived edema. The level of significance indicated is derived from LMMs to account for individual differences (* $p<0.05$ and ** $p<0.01$ compared to the <1% group, # $p<0.05$ and ## $p<0.01$ show significant differences between other paired groups; outliers not shown).

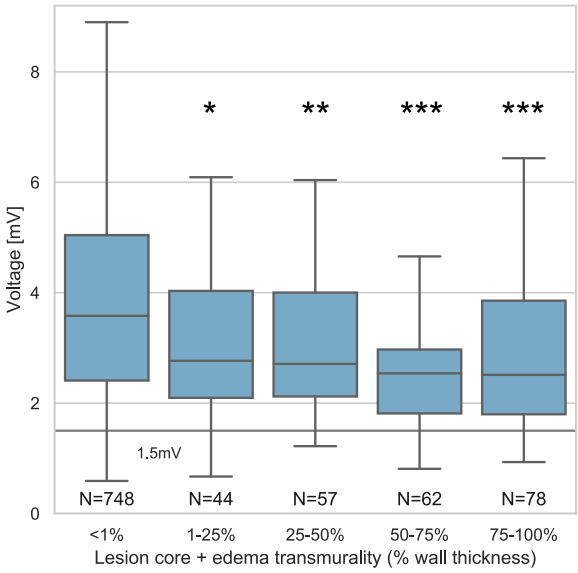

Fig. 4. Relationship between bipolar voltage and ablation lesion transmurality – Ablation transmurality included the combined T1-derived lesion core and T2-derived edema. Level of significance indicated is derived from the LMM to account for individual differences (* $p<0.05$, ** $p<0.01$, and *** $p<10^{-4}$ compared to the $<1\%$ transmurality group; no significant differences were detected between other paired groups; outliers not shown).

core and T2-derived edema pixels were significantly different from one another ($p \ll 0.05$; Wilcoxon rank sum test), but the 1-25% and 50-75% voltage measurements did not differ ($p>0.05$). These results indicate that the trend towards decreasing bipolar voltage with increasing proportions of T1-derived lesion core and T2-derived edema near the catheter tip are similar, and that while the T1-derived core is smaller (not reaching $>75\%$ in this study), the broader region of reduced voltage observed near RF lesions is a result of the presence of the T2-derived edema.

Using a similar LMM, bipolar voltage was also significantly reduced with the presence of the T1-derived lesion core and T2-derived edema, regardless of transmurality ($p<0.05$; Fig. 4). All voltage measurements with transmurality $>1\%$ were significantly reduced compared to the $<1\%$ group of measurements, and there was no significant difference detected between any other paired groups of measurements ($p>0.05$). Intersubject standard deviation was 0.36 mV.

D. Ex Vivo RF Lesion Characteristics

RF lesion diameters measured from T1-weighted MR and gross pathology were strongly correlated ($r=0.79$, $p=0.04$); diameters were not significantly over- or under-estimated by T1-weighted MR (bias$=1.0\pm1.5$ mm, $p=0.1$; 95% limits of agreement [–1.9, 4.0]). RF lesions measurements from gross pathology showed strong inter-observer agreement, with an ICC$=0.97$, Pearson's $r=0.98$ ($p \ll 0.01$), and bias$=0.24\pm0.44$ ($p>0.05$; 95% limits of agreement [–0.62, 1.11]).

In the core of thermal injury, Masson's Trichrome showed coagulative necrosis and loss of viability (blue stain; Fig. 5), and the corresponding H&E section revealed eosinophilic patches likely associated with denaturation of cytoplasmic proteins [30]. The lesion rim contained contraction band necrosis and hemorrhage. Evidence of injury was present beyond the lesion rim, with vacuolar degeneration and increased extracellular space compared to healthy tissue.

IV. Discussion

This study sought to characterize the permanent and transient injury caused by RF ablation using native-contrast MRI (representing tissue composition) in the LV, and assess the relationship to electrophysiological features (representing tissue function). MR provides visualization of the full myocardial wall, data which is not typically available in clinical ablation of the LV as EAM is a surfacic representation. In our study these datasets were inherently co-registered as they were both acquired in the same coordinate frame within the MR scanner.

The main findings resulting from this study are: (1) MR-derived RF lesions are associated with reduced bipolar voltage amplitude; (2) the presence of edema, indicated by elevated T2, contributed to reduced voltage; and (3) the T2-derived edema and T1-derived lesion core exhibited similar voltages. Together, these results suggest that while native-contrast MR can differentiate permanent RF lesions and transient edema, this is likely not possible using electrophysiological voltage measures alone.

A. Ablation-Induced Injury in the LV

In addition to the region of coagulative necrosis and short native T1 occurring where a lethal thermal dose is delivered [10], [31], microvascular injury, hemorrhage, ischemia, and edema also occur as a result of RF ablation (Fig. 5). Acute inflammatory edema accumulation increases the extracellular space and elevates T2 in MR in vivo, as seen in Fig. 5. Our hypothesis for the association with reduced bipolar voltage is that the cellular destruction at the permanent lesion created by ablation also leads to a redistribution of Na^+, Ca^{2+}, and K^+ ions (which define the transmembrane voltage of the nearby viable but edematous cells), ultimately leading to a temporary conduction block or potentially low tissue excitability.

The impact of varied extracellular volume and cell-to-cell coupling on electrical conduction have previously been explored in simulation and validated experimentally. Disrupted transverse cell coupling reduced conduction velocity and bipolar voltage in simulated monolayers of cells [32]. Similarly, experimental results showed decreased conduction velocity with an increase in extracellular space [33] and with upregulated expression of TNFα associated with the acute inflammatory cascade [34]. In this study, our findings of reduced bipolar voltage in edematous tissue could reflect similar changes to conduction velocity or wave front of activation near ablations [35], which would also be consistent with previous observations of conduction block with small gaps between RF lesions [36].

B. Resolution of MR and EP Measurements

Prior simulations and studies [27], [37], [38] showed that a catheter of approximately the size used in this study has a

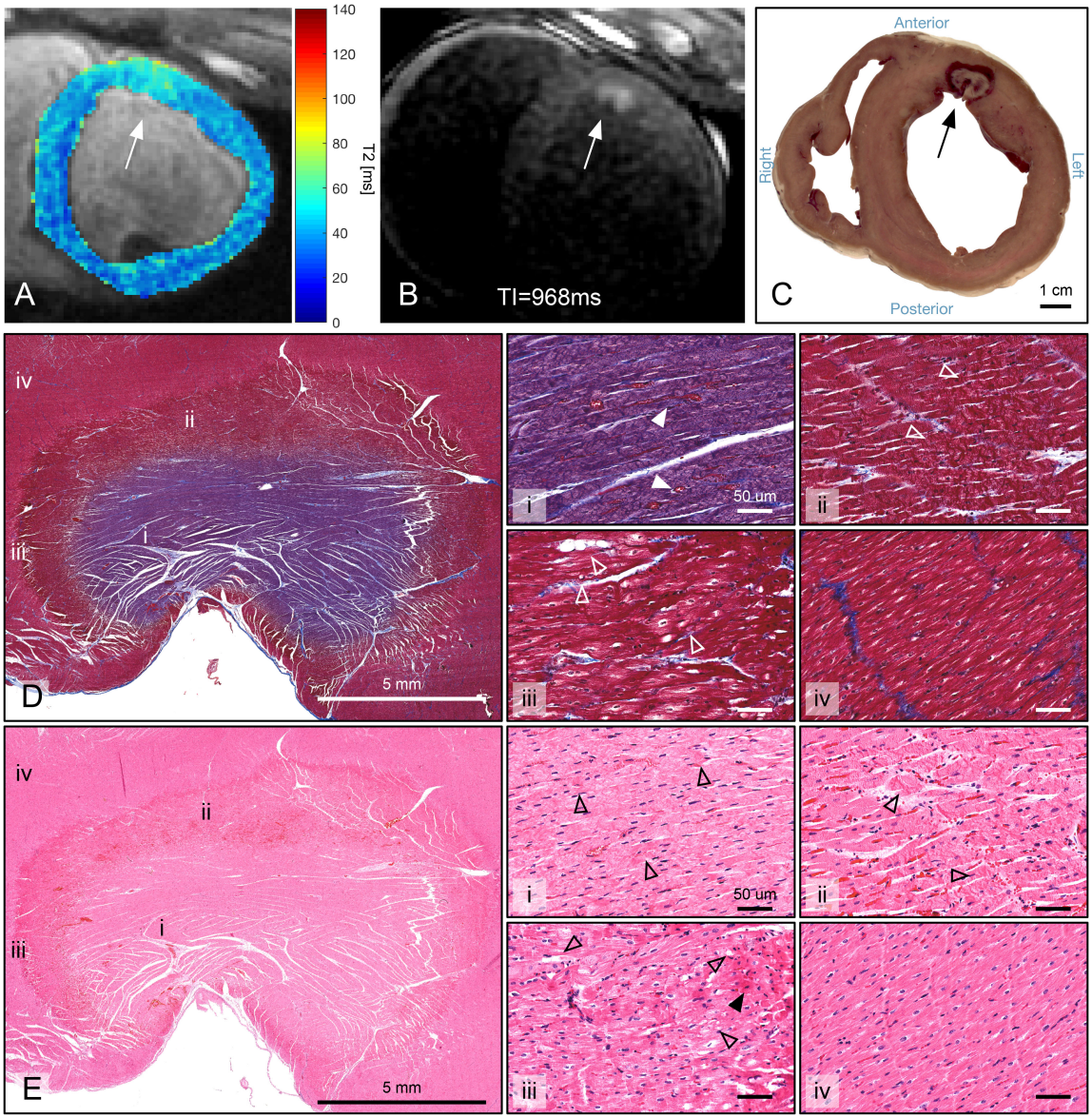

Fig. 5. Histological features of RF-induced injury - RF lesion in the anterior LV wall visualized in (A) T2 map and (B) T1-weighted IR-SSFP. (C) Gross pathology slice at a location corresponding to the MRI and cut in a similar short-axis orientation. Tissue sections stained with (D) MT and (E) H&E. (D) MT section with blue staining indicating non-viability of the RF lesion core. (D.i., E.i.) Magnification of coagulative necrosis in the lesion core. (D.i.) Congested microvasculature (solid arrows) and (E.i.) eosinophilic patches (open arrows) in cells possibly associated with denaturation of cytoplasmic proteins, seen throughout the lesion. (D.ii., E.ii.) Contraction band necrosis and hemorrhage in the lesion rim. (D.iii., E.iii.) Cell injury extending beyond the apparent lesion rim, with potentially necrotic eosinophilic cells (solid arrow), vacuolar degeneration (open arrows), and increased extracellular space compared to healthy myocardium (D.iv., E.iv).

sensitive FOV of roughly 6 mm in radius. Comparatively, the MR in-plane resolution was up to 4.8-fold higher than this catheter resolution, and provided depth-specific information within the LV wall. While catheter measurements necessitate choosing between small electrodes (which have higher resolution but less depth sensitivity) and larger electrodes (greater depth sensitivity but lower resolution), MR provides both full-thickness LV wall characterization and higher resolution.

The choice to use 2D MR imaging sequences in this study was reasonable considering the catheter FOV, although a more detailed delineation of RF lesions is expected with 3D acquisitions [13]. In future studies, we will move toward native-contrast MR with 1.5 mm isotropic resolution to capture features on the scale of conducting channels within VT reentry circuits [39], [40], particularly since the detection of these channels may be linked to image resolution [41].

C. MR-EP Alignment

In this study, MR images and catheter recordings were acquired with MR spatial encoding in the same coordinate frame and were inherently co-registered, without need for cross-modality registration. This approach reduces registration steps and sources of error compared to image integration with

commercial EAM systems. Despite a higher achievable precision with other commercial EAM systems (sub-millimeter, with reference catheter motion correction) [42], integrating MR image data introduces substantial registration error (reported at 3.83±0.57 mm and 3.8±0.8 mm) [43], [44], reducing overall accuracy.

Any potential misalignment due to physiological (cardiac and respiratory) motion throughout real-time catheter recordings was addressed by gating to diastole and end-expiration. This reduced the catheter positional uncertainty to an average SD of 2.2±0.9 mm. Considering the edema diameter of 26±8 mm and the RF lesion core diameter of 10±2 mm (Table II), we have sufficient accuracy to differentiate measurements made while the catheter was adjacent to edema or lesion core. Using the reported edema diameter and a 2-mm uncertainty in catheter location, catheter-based estimations of the extent of reduced voltage are associated with approximately 4-mm error in diameter (or 25% error in volume). Reducing the potential for alignment error is an ongoing topic of research in our lab, with current work focusing on dynamic models to correct intraprocedural device positioning in real time.

D. Limitations

A limitation of this study is the small number of RF lesions characterized. Since swine are prone to ventricular fibrillation during intracardiac procedures, 1–2 RF lesions each were delivered in this group of animals. Anti-arrhythmic medication was administered to minimize the potential for sudden cardiac events, but in some cases these events cut studies short (and accounted for the subset of animals without LGE imaging). Contact force sensing catheters were not available to be used for this study, and we acknowledge this as a limitation of the voltage measurements; bipolar voltage is known to be sensitive to catheter-myocardium contact (among other factors).

EGM waveforms were used as an indicator of catheter-myocardium contact and stability, but were primarily used quantitatively for bipolar voltage measurements in this analysis (as these were the most robust measurements provided by this early generation of our MR-EP system). Adding confidence to our measurements of bipolar voltage, the healthy myocardial voltages were similar to the voltage distributions used previously to define the $<$1.5 mV threshold for identifying scar [28], [29]. In this study, voltages measured in ablated tissue ranged predominantly between 1.5 mV and 3 mV, a threshold used non-specifically to define abnormal tissue [28], [29]. The catheter electrode size and small sample sizes could have contributed to the non-significant difference between bipolar voltage measured in the RF lesion cores and edema.

While absolute precision of catheter tip position determined by using the real-time MR-guided EP system is slightly lower than that reported for EAM systems (e.g., Carto3), overall misregistration between MR images and EP data appears lower with MR guidance of the ablation procedure. A limitation of this study is that it lacks a strong verification of catheter contact (unlike other EAM systems which include contact force sensing), although contact was inferred by EGM waveform and tissue proximity. The resulting RF lesion cores were of similar dimensions compared to those created with contact force sensing in a similar model [45]. Previous work found a small increase in RF lesion size with increasing contact force, but comparatively large enhancement of the edematous volume [46], which suggests that inconsistent contact force could be a cause of variability in edema extent seen in the current study.

E. Role of MRI in Clinical Ablation

There remains a need for robust intraprocedural lesion assessment during VT ablation cases, as is highlighted by observations of unpredictable lesion formation especially near myocardial fat or fibrosis [45], [47]. MR visualization provides detailed assessment of lesion severity and extent [9], [11], [15]. Specifically, native T1-weighted MR provides detailed visualization of lesion extent, even in the presence of myocardial tissue inhomogeneity (including fat and fibrosis) [45]. This technique has been validated through correlations between histological necrosis and T1-derived lesion cores both in the current study and in the literature [10], [15], [45].

Our results suggest that the relatively larger volume of edema masks the smaller permanent RF lesion, and that electrophysiology-based measures could overestimate the extent of the permanent lesion. Our analysis of the MR image pixels near the catheter tip and lesion transmurality indicate that native-contrast MRI provides additional sensitivity to lesion depth, which is not adequately reflected by changes in bipolar voltage. These findings motivate an ablation strategy which seeks to create large contiguous permanent RF lesions while minimizing the formation of edema, or to deliver multiple RF lesions before significant edema develops.

In future studies of technical developments for optimizing ablation strategies, MRI-guided ablation (as used in this study) could be implemented for in vivo validation of complementary intraprocedural lesion assessment techniques, such as real-time 3D lesion modeling [48]. The findings from the current study provide grounds for further investigation of RF lesion creation as a function of ablation parameters and protocols, with the aim of maximizing the permanent T1-derived lesion extent while reducing transient T2-derived edema development to minimize VT recurrence. Moving towards 3D or higher resolution native-contrast T1- and T2-based MRI acquisitions would facilitate such investigations.

Future ablation procedures performed fully under MRI guidance could incorporate lesion assessment intra-procedurally, during a time window when additional ablations may be delivered. Cases of inadequate reentry circuit ablation (identified using native T1-weighted MRI) could facilitate immediate targeted re-ablation to thoroughly eliminate any remaining conducting channels. Integrating native-contrast MRI lesion visualization into ablation procedures has the potential to improve efficacy (lower the rates of recurrence) and reduce the need for follow-up procedures.

In clinical VT ablation performed in a conventional EP lab (not under MRI guidance), post-procedure MR lesion assessment could facilitate interpretation of procedure endpoints or

even constitute new endpoints. In this scenario, structurally-defined conducting channels comprising the suspected reentry circuits could be delineated in advance using 3D LGE, then targeted for ablation in the EP lab. When conduction is blocked in these reentry circuits after ablation, native-contrast MR could confirm whether permanent lesions or transient edema are present. Any channels not transected by permanent RF lesions could then be targeted for additional ablation. The presence of edema could mask remaining conducting channels critical for VT and could confound electrophysiological ablation endpoints. Future work could explore the role of MR lesion assessment early after clinical VT ablation to guide decision making for follow-up procedures and predict durable reentry circuit blockage based on the presence of permanent lesions. These findings may be used to support the important emerging role of MRI in assessing ablation and understanding the mechanisms for VT recurrence.

V. Conclusion

After RF ablation in the LV, reduced bipolar voltage was observed at the site of the permanent RF lesion and surrounding edematous tissue as derived from intraprocedural native-contrast MRI. The permanent lesion and transient edema are distinct in MR images, but not differentiable with bipolar voltage. These results are significant in the context of MR-guided ablation procedures, whose clinical application is now feasible.

References

[1] P. Vergara *et al.*, "Predictive score for identifying survival and recurrence risk profiles in patients undergoing ventricular tachycardia ablation: The I-VT score," *Circ. Arrhythm. Electrophysiol.*, vol. 11, no. 12, pp. 1–12, Dec. 2018.

[2] J. Mallidi *et al.*, "Meta-analysis of catheter ablation as an adjunct to medical therapy for treatment of ventricular tachycardia in patients with structural heart disease," *Heart Rhythm*, vol. 8, no. 4, pp. 503–510, 2011.

[3] B. R. Knowles *et al.*, "3-D visualization of acute RF ablation lesions using MRI for the simultaneous determination of the patterns of necrosis and edema," *IEEE Trans. Biomed. Eng.*, vol. 57, no. 6, pp. 1467–1475, Jun. 2010.

[4] G. R. Vergara and N. F. Marrouche, "Tailored management of atrial fibrillation using a LGE-MRI based model: From the clinic to the electrophysiology laboratory," *J. Cardiovasc. Electrophysiol.*, vol. 22, no. 4, pp. 481–487, Apr. 2011.

[5] T. Yamada *et al.*, "Incidence, location, and cause of recovery of electrical connections between the pulmonary veins and the left atrium after pulmonary vein isolation," *Europace*, vol. 8, no. 3, pp. 182–188, 2006.

[6] A. Arujuna *et al.*, "Acute pulmonary vein isolation is achieved by a combination of reversible and irreversible atrial injury after catheter ablation: Evidence from magnetic resonance imaging," *Circ. Arrhythm. Electrophysiol.*, vol. 5, no. 4, pp. 691–700, Aug. 2012.

[7] H. Ghanbari *et al.*, "Noninducibility in postinfarction ventricular tachycardia as an end point for ventricular tachycardia ablation and its effects on outcomes: A meta-analysis," *Circ. Arrhythm. Electrophysiol.*, vol. 7, no. 4, pp. 677–683, Aug. 2014.

[8] A. C. Lardo *et al.*, "Visualization and temporal/spatial characterization of cardiac radiofrequency ablation lesions using magnetic resonance imaging," *Circulation*, vol. 102, no. 6, pp. 698–705, Aug. 2000.

[9] R. Ranjan *et al.*, "Identification and acute targeting of gaps in atrial ablation lesion sets using a real-time magnetic resonance imaging system," *Circ. Arrhythm. Electrophysiol.*, vol. 5, no. 6, pp. 1130–1135, Dec. 2012.

[10] H. Celik *et al.*, "Intrinsic contrast for characterization of acute radiofrequency ablation lesions," *Circ. Arrhythm. Electrophysiol.*, vol. 7, no. 4, pp. 718–727, 2014.

[11] E. Ghafoori *et al.*, "Characterization of gadolinium contrast enhancement of radiofrequency ablation lesions in predicting edema and chronic lesion size," *Circ. Arrhythm. Electrophysiol.*, vol. 10, no. 11, pp. 1–9, Nov. 2017.

[12] E. G. Kholmovski *et al.*, "Acute noncontrast T1-weighted magnetic resonance imaging predicts chronic radiofrequency ablation lesions," *J. Cardiovasc. Electrophysiol.*, vol. 29, no. 11, pp. 1556–1562, Nov. 2018.

[13] M. A. Guttman *et al.*, "Non-contrast-enhanced T1-weighted MRI of myocardial radiofrequency ablation lesions," *Magn. Reson. Med.*, vol. 79, no. 2, pp. 879–889, Feb. 2018.

[14] K. Farahani *et al.*, "MRI of thermally denatured blood: Methemoglobin formation and relaxation effects," *Magn. Reson. Imag.*, vol. 17, no. 10, pp. 1489–1494, Dec. 1999.

[15] M. A. Guttman *et al.*, "Acute enhancement of necrotic radio-frequency ablation lesions in left atrium and pulmonary vein ostia in swine model with non-contrast-enhanced T1-weighted MRI," *Magn. Reson. Med.*, vol. 83, no. 4, pp. 1368–1379, Apr. 2020.

[16] P. R. P. Krahn *et al.*, "Cardiovascular magnetic resonance guided ablation and intra-procedural visualization of evolving radiofrequency lesions in the left ventricle," *J. Cardiovasc. Magn. Reson.*, vol. 20, no. 1, pp. 1–12, 2018.

[17] P. Krahn *et al.*, "MRI-based myocardial ablation lesion extent relates to area of voltage reduction in MR-guided electroanatomical voltage maps," in *Proc. Int. Soc. Magn. Reson. Med.*, 2017, pp. 1–12.

[18] P. Krahn *et al.*, "Combined MR visualization and electrophysiological characterization of RF lesions in the left ventricle," in *Proc. Heart Rhythm Sci. Sess.*, 2019, p. S296.

[19] P. Krahn *et al.*, "Relationship between CMR visualization and electrophysiological properties of acute RF lesions in the left ventricle," in *Proc. Soc. Cardiovasc. Magn. Reson.*, 2019, pp. 468–470.

[20] S. O. Oduneye *et al.*, "The feasibility of endocardial propagation mapping using magnetic resonance guidance in a swine model, and comparison with standard electroanatomic mapping," *IEEE Trans. Med. Imag.*, vol. 31, no. 4, pp. 977–983, Apr. 2012.

[21] H. Chubb *et al.*, "Development, preclinical validation, and clinical translation of a cardiac magnetic resonance-electrophysiology system with active catheter tracking for ablation of cardiac arrhythmia," *JACC Clin. Electrophysiol.*, vol. 3, no. 2, pp. 89–103, Feb. 2017.

[22] C. L. Dumoulin *et al.*, "Real-time position monitoring of invasive devices using magnetic resonance," *Magn. Reson. Med.*, vol. 29, no. 3, pp. 411–415, Mar. 1993.

[23] P. E. Radau *et al.*, "VURTIGO: Visualization platform for real-time, MRI-Guided cardiac electroanatomic mapping," *Lecture Notes Comput. Sci.*, vol. 7085, pp. 244–253, 2012.

[24] N. R. Ghugre *et al.*, "Quantitative tracking of edema, hemorrhage, and microvascular obstruction in subacute myocardial infarction in a porcine model by MRI: Quantitative tracking of edema, hemorrhage, and MVO," *Magn. Reson. Med.*, vol. 66, no. 4, pp. 1129–1141, Oct. 2011.

[25] J. Detsky *et al.*, "Inversion-recovery-prepared SSFP for cardiac-phase-resolved delayed-enhancement MRI," *Magn. Reson. Med.*, vol. 58, no. 2, pp. 365–372, Aug. 2007.

[26] N. R. Ghugre *et al.*, "MRI detects myocardial iron in the human heart," *Magn. Reson. Med.*, vol. 56, no. 3, pp. 681–686, Sep. 2006.

[27] S. O. Oduneye *et al.*, "Post-infarction ventricular tachycardia substrate characterization: A comparison between late enhancement magnetic resonance imaging and voltage mapping using a MR-guided electrophysiology system," *IEEE Trans. Biomed. Eng.*, vol. 60, no. 9, pp. 2442–2449, Sep. 2013.

[28] D. M. Cassidy *et al.*, "The value of catheter mapping during sinus rhythm to localize site of origin of ventricular tachycardia," *Circulation*, vol. 69, no. 6, pp. 1103–1110, Jun. 1984.

[29] F. E. Marchlinski *et al.*, "Linear ablation lesions for control of unmappable ventricular tachycardia in patients with ischemic and nonischemic cardiomyopathy," *Circulation*, vol. 101, no. 11, pp. 1288–1296, Mar. 2000.

[30] V. Kumar *et al.*, *Robbins and Cotran Pathologic Basis of Disease*, 8th ed. New York, NY, USA: Elsevier, 2009.

[31] S. Toupin *et al.*, "Feasibility of real-time MR thermal dose mapping for predicting radiofrequency ablation outcome in the myocardium in vivo," *J. Cardiovasc. Magn. Reson.*, vol. 19, no. 14, pp. 1–12, Dec. 2017.

[32] V. Jacquemet and C. S. Henriquez, "Genesis of complex fractionated atrial electrograms in zones of slow conduction: A computer model of microfibrosis," *Heart Rhythm*, vol. 6, no. 6, pp. 803–810, Jun. 2009.

[33] R. Veeraraghavan *et al.*, "Interstitial volume modulates the conduction velocity-gap junction relationship," *Amer. J. Physiol. Heart Circ. Physiol.*, vol. 302, no. 1, pp. H278–H286, Jan. 2012.

[34] S. A. George *et al.*, "TNF modulates cardiac conduction by altering electrical coupling between myocytes," *Front. Physiol.*, vol. 8, no. 334, pp. 1–13, May 2017.
[35] M. E. Josephson and E. Anter, "Substrate mapping for ventricular tachycardia: Assumptions and misconceptions," *JACC Clin. Electrophysiol.*, vol. 1, no. 5, pp. 341–352, Oct. 2015.
[36] R. Ranjan *et al.*, "Gaps in the ablation line as a potential cause of recovery from electrical isolation and their visualization using MRI," *Circ. Arrhythm. Electrophysiol.*, vol. 4, no. 3, pp. 279–286, Jun. 2011.
[37] J. M. Stinnett-Donnelly *et al.*, "Effects of electrode size and spacing on the resolution of intracardiac electrograms," *Coron. Artery Dis.*, vol. 23, no. 2, pp. 126–132, Mar. 2012.
[38] S. Misra *et al.*, "Field of view of mapping catheters quantified by electrogram associations with radius of myocardial attenuation on contrast-enhanced cardiac computed tomography," *Heart Rhythm*, vol. 15, no. 11, pp. 1617–1625, Nov. 2018.
[39] H. Ashikaga *et al.*, "Magnetic resonance based anatomical analysis of scar-related ventricular tachycardia: Implications for catheter ablation," *Circ. Res.*, vol. 101, no. 9, pp. 939–947, Oct. 2007.
[40] D. Andreu *et al.*, "3D delayed-enhanced magnetic resonance sequences improve conducting channel delineation prior to ventricular tachycardia ablation," *Europace*, vol. 17, no. 6, pp. 938–945, Jun. 2015.
[41] M. Pop *et al.*, "High-resolution 3-D T1*-mapping and quantitative image analysis of GRAY ZONE in chronic fibrosis," *IEEE Trans. Biomed. Eng.*, vol. 61, no. 12, pp. 2930–2938, Dec. 2014.
[42] L. Gepstein *et al.*, "A novel method for nonfluoroscopic catheter-based electroanatomical mapping of the heart: In vitro and in vivo accuracy results," *Circulation*, vol. 95, no. 6, pp. 1611–1622, Mar. 1997.
[43] A. P. Wijnmaalen *et al.*, "Head-to-head comparison of contrast-enhanced magnetic resonance imaging and electroanatomical voltage mapping to assess post-infarct scar characteristics in patients with ventricular tachycardias: Real-time image integration and reversed registration," *Eur. Heart J.*, vol. 32, no. 1, pp. 104–114, Jan. 2011.
[44] S. Gupta *et al.*, "Delayed-enhanced MR scar imaging and intraprocedural registration into an electroanatomical mapping system in post-infarction patients," *JACC Cardiovasc. Imag.*, vol. 5, no. 2, pp. 207–210, Feb. 2012.
[45] S. Tao *et al.*, "Ablation lesion characterization in scarred substrate assessed using cardiac magnetic resonance," *JACC Clin. Electrophysiol.*, vol. 5, no. 1, pp. 91–100, Jan. 2019.
[46] S. Thomas *et al.*, "Higher contact force during radiofrequency ablation leads to a much larger increase in edema as compared to chronic lesion size," *J. Cardiovasc. Electrophysiol.*, vol. 29, no. 8, pp. 1143–1149, 2018.
[47] M. Barkagan *et al.*, "Histopathological characterization of radiofrequency ablation in ventricular scar tissue," *JACC Clin. Electrophysiol.*, vol. 5, no. 8, pp. 920–931, Aug. 2019.
[48] C. Linte *et al.*, "Lesion modeling, characterization, and visualization for image-guided cardiac ablation therapy monitoring," *J. Med. Imag.*, vol. 5, no. 2, Apr. 2018, Art. no. 021218.